33RD CONGRESS
OF THE INTERNATIONAL COUNCIL
OF THE AERONAUTICAL SCIENCES
STOCKHOLM, SWEDEN, 4-9 SEPTEMBER, 2022

ICAS 2022 SWEDEN

Aeronautical CFD and Turbulence – Progress and Challenges

Arthur Rizzi[1] & Dan Henningson[1]

[1]Department of Engineering Mechanics, KTH Royal Institute of Technology

Abstract

Separated flows often set aerodynamic limits for an aircraft flight envelope, and many of these flows remain difficult to predict with Computational Fluid Dynamics (CFD). This paper reviews and explores how CFD simulations have been used for predicting separated flows, and the associated aerodynamic performance, throughout the flight envelope, giving special focus to military aircraft. The review entails: a summary of the physics of flow separation that is especially difficult to model accurately; an historical sketch of seven decades of CFD developments to meet many of the challenges of separated flow predictions; three case studies for an assessment of the current CFD capabilities; and future prospects for further improvements in the CFD simulations using direct numerical simulations (DNS). DNS can be utilized as a virtual wind tunnel to understand complex separated flow and the results used in modelling improvements for RANS and LES CFD methods. Several examples of the capabilities of DNS methods to predict separated aeronautical flows are given. However, significant advances are still needed for separated flow simulations to become practical with reliability comparable to those of attached flow simulations. A possible path forward for future work to achieve this goal is included.

Keywords: Separated flow, vortices, Large Eddy Simulation, Direct Navier-Stokes solution, swept wing

1. Introduction

Over the last 60 years, the use of Computational Fluid Dynamics (CFD) in industrial airframe design has grown such that today CFD codes solving the Navier–Stokes equations have become standard tools in aircraft analysis and design. Navier–Stokes codes also are being embedded increasingly in a numerical multi-disciplinary analysis and design environment to enable computation based optimal aircraft design including aeroelastic flexibility of wings and thermal effects of engine heat transfer. CFD has grown from a tool used to supplement wind tunnel or flight experiments to an identifiable new technology standing on its own, making important contributions to all stages of the design of a flight vehicle. Looking back on those 60 years' experience in using CFD to predict the forces, moments and loads on the flight vehicle over a wide range of flight conditions within good engineering accuracy reveals the enormous progress made. Three factors were instrumental in this: (1) the increase in available computer resources, (2) the progress in development of efficient numerical methods, and (3) the progress in physical modeling.

At ICAS 1990 in Stockholm the Guggenheim Award Lecture by Prof. Mårten Landahl had the title “CFD and Turbulence”[1]. The present talk will survey some main developments in CFD and DNS of aeronautically relevant flows since then.

The three past decades of experience developing RANS methods has produced very effective aeronautical CFD tools for attached flow simulations. It has also brought about the maturation of Direct Numerical Simulation (DNS) methods for studying the physics of turbulence and transition without modelling. RANS technology today accurately predicts forces and moments for design conditions when the flow field is steady and the turbulent boundary layer remains attached over the aircraft surface.

Wall-bounded turbulence models are adequate to treat this class of flow to required engineering precision. Accurate predictions are also made when a vortex is shed from a sharp-edged swept wing and remains concentrated over the vehicle, i.e. when the relevant vortical flow details remain large scale and the turbulence-scales have only insignificant effects on the vehicle performance.

In some circumstances separated transitional and turbulent flows, however, often set aerodynamic limits for an aircraft flight envelope, for example the stalling characteristics encountered as maximum lift is approached is information the designer uses to build a better aircraft. Predictions become less reliable, however, when the turbulent boundary layer separates before the tail of the vehicle and becomes unsteady over its surface. Through nonlinear dynamics large-scale flow features breakdown into finer and finer scales. The turbulence is no longer wall-bounded and RANS turbulence models become unreliable. Thus, many of these flows remain difficult to predict to an acceptable level of certainty with traditional Computational Fluid Dynamics.

Other authors have reviewed aspects of these developments extensively, see for recent examples references [2,3,4]. Hirschel et al.[5] explain and elaborate these types of phenomena, their modeling and computation, at book-length. Here only a brief summary is given in order to set the stage of the current use of CFD in aircraft design.

1.1 History of CFD development and application

The advent of jet propulsion in the late 1940s brought high-speed flight, shock waves on swept and low aspect ratio configurations where separation, as a phenomenon, branched out in several directions from classical boundary-layer separation on an unswept wing to controlled vortex separation, shock-induced separation, etc.

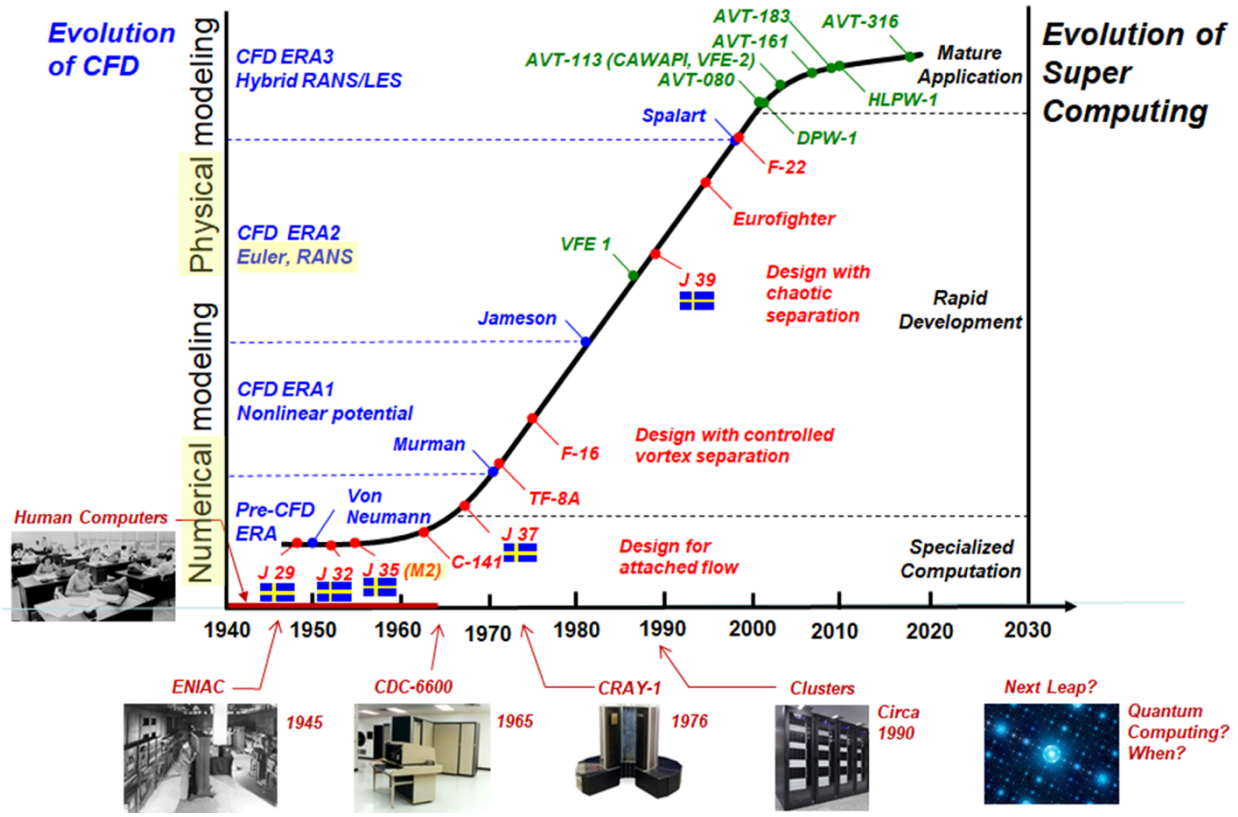

Figure 1 - Seven decades of CFD development.

Major driving forces for the rapid development of CFD has been the need for aerodynamic prediction methods for the transonic speed range, in which nonlinear effects and shock waves appear, and the interest in flows containing strong separated vortices which show up at large angles attack for highly

swept wings. Appearing in the late 1940s and early 1950s, jet-propelled fighters required thin wings in slender configurations with swept leading edge – high sweep meant lower high-speed drag but also generated less lift. However, it was discovered that separation from a sufficiently swept leading edge created a stable vortex over the wing that enhances the lift, and this effect is widely exploited in all designs. Flows with “coherent vortex separation” then lead to new nonlinear interaction phenomena, such as: vortex breakdown stall, shock-vortex interaction and shock-vortex-boundary layer interactions (SVBLI) of many variants.

Figure 1 presents an historical sketch for seven decades of CFD development [2]. CFD entails a marriage of theoretically-based numerical solution techniques with scientific computing capacity, and, on this figure, we juxtapose the evolution of CFD (subdivided into eras) with the evolution of supercomputing (also subdivided). The figure also includes select aircraft (first flight date) and, in green, collaborative CFD ventures to assess current prediction capability (initiation date).

ERA-2 is based on the solution of the Euler (and shortly thereafter Reynolds-averaged Navier-Stokes (RANS)) equations and was established by Jameson’s theoretical work in 1981. Landahl reviewed this progress up to 1990 and in addition, Vos et al.[4] extensively reviewed, from a European perspective, the ERA-2 RANS CFD technology for numerous problems in aircraft design up to year 2000. The major tool then was RANS using standard wall-bounded turbulence models. At the same time, as Landahl explained, advances in numerical modelling also brought the possibility to solve the Navier-Stokes equations for all the turbulent scales without the need for modelling, but such DNS at that time were limited by the size of the supercomputers to flows of rather low Reynolds number and simple geometries.

ERA-3 is based on the solution of unsteady flows with hybrid RANS/Large-Eddy-Simulation (LES) techniques and was established by the theoretical work of Spalart et al.[6] in 1997 pioneering the concept of detached eddy simulation. This era saw the mature application of scientific cluster computing, but it also has seen a decline in the ability of scientific computing capacity to meet contemporary CFD needs. Vos et al.[4] also discussed several early unsteady flow applications using DES physical modeling. The size and speed of supercomputers progressively increased allowing an increase in the Reynolds number of flows studied by DNS.

Throughout these seven decades, CFD development has taken the form of climbing a ladder of ever-increasing physics simulation and, along the way, expanding the ability to represent geometric complexity for aircraft applications. Much of this work was enabled, in part, by rapid advancements in supercomputer capability. An assessment of the reliability of the physical modelling used in these collective CFD techniques are described in the following sections.

RANS simulations of separated flows apparently have reached a level of diminishing returns as regards new capability and certainty, and that many of the present CFD simulation challenges for separated flows will require at least hybrid RANS/LES technology and even higher levels of physical modelling. The ubiquitous challenge here is turbulence, with transition equally challenging but in question only in relatively small regions and in special applications. Progress will be dependent on new ideas and their correct implementation, where direct numerical simulation (DNS) studies can play a crucial role to advance the understanding of the underlying flow physics. Recent advances in DNS methodology and increased computer capacity now allow the physics of aeronautical flow fields to be computed on first principles instead of assumed models. DNS can accurately predict the separation, the laminar-turbulent transition and the often very sensitive interplay between these phenomena. Using modern DNS methods and the largest high-performance computers these calculations can now be performed in typical flow situations of university wind tunnels, i.e. making the calculations effectively act as a virtual wind tunnel. The DNS calculations are still limited to rather low Reynolds numbers and low Mach numbers and are therefore often used to study flow physics phenomena that is of importance to model in CFD calculations.

1.2 Organization of paper

This lecture consists of two parts. Part 1 addresses how CFD simulations have been used for predicting separated flows in practical applications, and the associated aerodynamic performance of the vehicle throughout its flight envelope, giving special focus to actual aircraft. It entails a summary of the physics of flow separation that is especially difficult to model numerically, pointing to DNS studies that shed new light on the physics and that lay out a path for substantial progress in physical modeling. Among the cases reviewed in Part 1 are: turbulent separation from a smooth-surface including short laminar-turbulent bubbles, incipient vortex separation including static and dynamic bursting, buffet onset and stalling characteristics. Using DNS computations as virtual wind tunnel, Part 2 highlights the flow physics of unsteady separation for pitching wings undergoing small oscillations, and for dynamic stall of airfoils. The aim is to understand the underlying flow physics so that better models can be obtained when such flows are modelled in unsteady CFD calculations. The last section aims at unifying the two parts, showing how the detailed DNS can be used to improve the models needed for the calculations presented in the first part.

2. Separated Flow Inhibits CFD Reliability over broader Flight Envelope

Accurate prediction of separated flows has proved a significant challenge to CFD. The impression is that physical model development – for separated flows as well as transition from laminar to turbulent flow - has stalled and is a bottleneck.

It is now the case that wings are designed using CFD, and confirmed in the wind tunnel, and that very few wings are tested. CFD predicts flows in cruise conditions to engineering accuracy, as witness the progress demonstrated in the "Drag Prediction" workshops [7]. But outside the cruise range, separated flows are the norm, and there is less confidence in CFD: RANS models with current turbulence models have been found unreliable.

This is discussed in terms of the maneuver, or *V-n*, diagram in Figure 2. It indicates the intended operating range within the flight envelope of high speed aircraft, and suggests the flow physics that may pertain to its aerodynamic performance as a function of speed and lift generated in terms of multiple *g* weight forces. Consider a vertical line at a given speed: at B, cruise, there is lift of 1*g* for level unaccelerated flight, i.e. the linear range of the C_L vs α diagram within Figure 2. For rapid pull-up, the pilot commands higher incidence, more lift of say 3*g* at C for combat and maneuver, and in so doing may encounter the onset of buffet because C is near max lift and stall in the C_L vs α diagram. In another scenario, a horizontal line in the diagram, the pilot may command higher speed at a given lift, say 2*g*, at D for supersonic operations, and may well encounter strong shock effects like shock stall. High lift devices are needed for take-off and landing operations, location A, where confluent flows, possibly with transition effects, come into play.

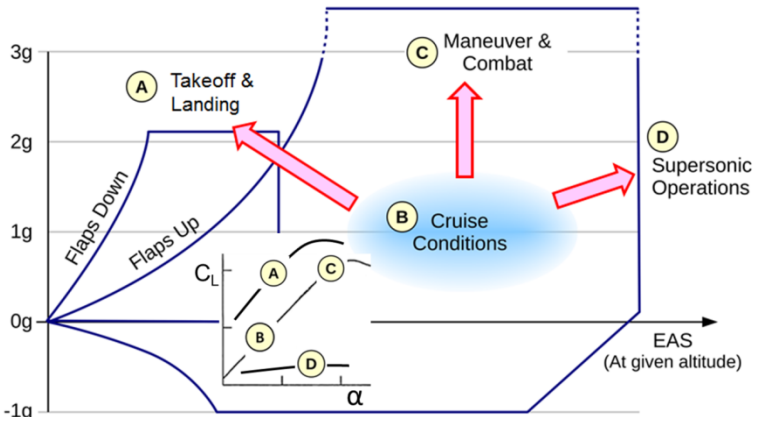

Figure 2 - Separated flow occurs on boundaries of envelope in maneuver diagram.

2.1 Cruise condition prediction progress

The CFD Drag Prediction Workshop Series (Cruise Condition) publishes geometries and invites CFD predictions of drag for cruise conditions ((B) in Figure 2) typical of current airliner clean configurations. The workshops attract a large number of participants and provides ample data for comparison of different codes, turbulence models, and grids. Figure 3 illustrates the progress from DPW 1 to DPW5 [7]. Current predictions statistics show a couple drag counts in standard deviation. The progress follows from increasing grid resolution, improved physical modeling, and culling of models that have systematically underperformed.

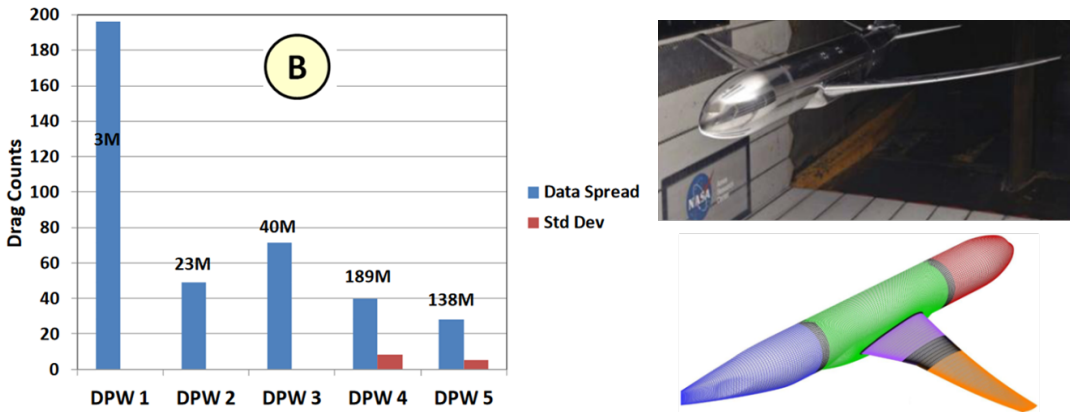

Figure 3 - CFD Drag Prediction Workshop series shows reduction in data spread and standard deviation in predicted drag (cruise condition) [7].

RANS codes use standard wall-bounded turbulence models designed for attached boundary layers. If the boundary layer should separate before the trailing edge, use of such models is questionable. To address this issue, Spalart [6] proposed the concept of the DES (Detached Eddy Simulation) Model, Figure 4) that injects eddies, computed by RANS near the wall, and then follows them with LES methodology as they propagate outward into the exterior flow field. The primary advantage with a hybrid RANS/LES method is that it resolves geometry-dependent, unsteady three-dimensional turbulent motions away from the wall with the LES methodology.

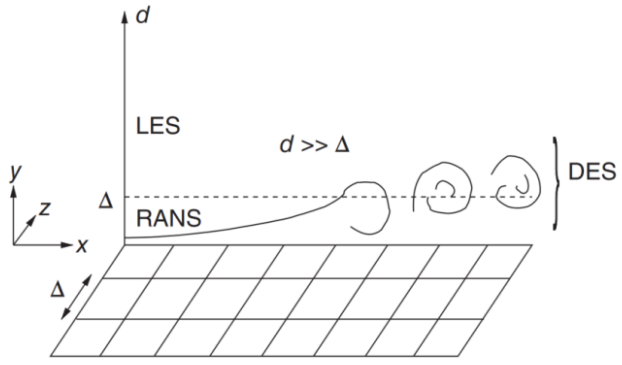

Figure 4 - Detached-eddy simulation, a hybrid RANS-LES methodology

The following sections assess the current capabilities of RANS/DES and contrast them to direct numerical simulation (DNS) computations used as a virtual wind tunnel. First we address the flow physics of slender delta wings.

3 Flow Physics of Slender Delta Wings

For wings of high sweep and thin profiles, separation likely takes place near the leading edge, and here the notion of bubble type may not hold. Instead, separation in this case implies that wall-streamlines on the body leave the surface and continue into the flowfield as a vortex layer/sheet that, under self-induction, rolls up into a vortex, see Figure 5 [8]. If the leading edge of the wing is sharp, this geometrical feature fixes the location where the vortex sheet leaves the surface, and the flow could be handled as an inviscid computation.

3.1 Incipient vortex separation from smooth surface

But when the leading-edge radius is finite, the location where the vortex sheet is formed is far from obvious and three-dimensional boundary layer separation must be resolved. The origin of the primary leading-edge vortex varies with angle of attack, and an additional vortical structure arises inboard on the wing in association with the leading-edge vortex separation, Figure 5. The AVT-113 task group [9] analyzed the flow features denoted in Figure 5 on a 65°-swept delta wing in a project known as Vortex Flow Experiment 2 (VFE-2), and the AVT-183 task group [10] analyzed this flow on a 53°-swept diamond wing in a validation-motivated approach. Both activities combined new wind tunnel measurements and CFD computations. The resounding conclusion is that details of flow separation along a blunt swept-wing leading edge are extremely sensitive to the numerical and physical modeling approach taken.

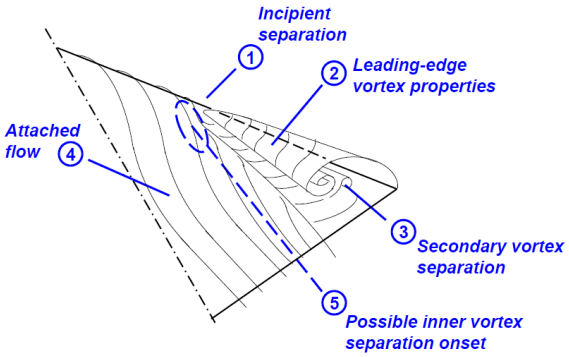

Figure 5 - Smooth-surface separation, delta wings [8].

3.1.1 Phenomenological notion of leading-edge separation

We have mentioned two broadly descriptive notions of separation: bubble-like and vortex-shear (sheet) separation, both of which occur from smooth surfaces. Although separation is an inherently 3D phenomenon, it is nevertheless useful, and easier, to discuss bubble separation in a 2D context

Figure 6 sketches the leading-edge separation, and physics, which occur on an airfoil as summarized by Polhamus [11]. For leading-edge stall (Figure 6), leading-edge separation occurs but with a short bubble that contracts with angle of attack (A). At some angle of attack (B), the pressure gradient in the leading-edge region becomes sufficient to cause turbulent reseparation along with an abrupt loss of lift. At still higher alpha (C) the separated turbulent flow develops into a vortex, see Section 5.3.1 for the scale-resolving computations detailing the flow physics.

The separated flow physics indicated in Figure 6 for two-dimensional airfoils are pertinent to three-dimensional wings by accounting for aspect ratio and sweep effects on airfoil loading (Polhamus [11]). Applications to the straight wing involve finite aspect ratio effects and seem relatively straightforward, but further discussion is warranted for sweep effects. In simplified form, Figure 7 presents two primary phenomena that arise with increasing sweep angle. The spanwise pressure gradient along the leading edge sweeps the turbulent reseparation and resulting expanding long bubble outboard as shown in the left portion of Figure 7. For wings of moderate-to-high sweepback these spanwise pressure gradients

can be of sufficient magnitude to convert the expanding long bubble flow into the vortex flow illustrated in the right sketch of Figure 7. Additional insights for swept-wing flow characteristics can be found in Küchemann [12] and in the textbook by Rizzi and Oppelstrup [13].

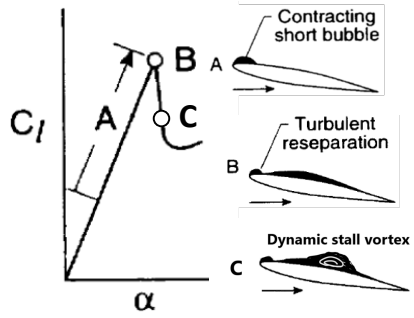

Figure 6 - Airfoil leading-edge stall

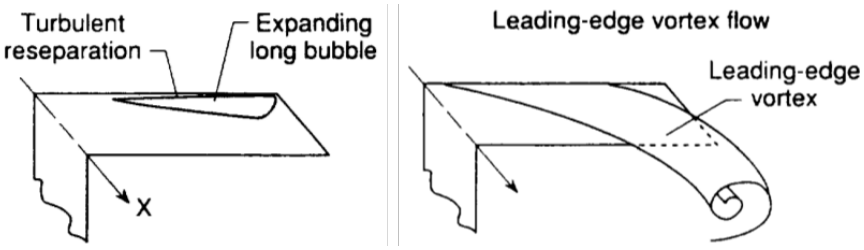

Figure 7 - Sweptback wing flow separation and leading-edge vortex flow features. Polhamus[11].

3.2 Vortex Breakdown

At moderate angles of attack, a steady well-ordered vortex develops that enhances the lift of the delta wing. This vortex-enhanced lift increases with increasing angle of attack until the vortex suddenly "bursts" or breaks down into more chaotic rotational motion Figure 8a , at which point $C_{L,max}$ has been reached Figure 8b.

The term bursting or breakdown of a vortex refers to the structural change from a strong regular spiral motion to a weaker turbulent motion which can occur at some position along a vortex. Low-speed windtunnel investigations [14] of vortex flows generated from sharp, swept back leading edges have recorded various observations of this phenomenon, Figure 10a. These reveal a sudden deceleration of fluid along the vortex axis and expansion of the vortex around a stagnant core downstream of which the flow is turbulent; it is possible at very low stream velocity to see the axial flow, after deceleration, deflect and perform a regular whirling motion before turbulent breakdown, depicted in Figure 10. The vortex bursts above the wing when the adverse pressure gradient occurring at the trailing edge becomes sufficiently large.

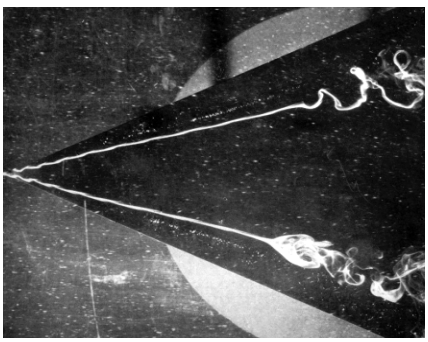

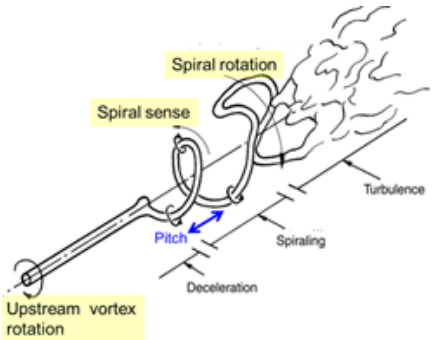

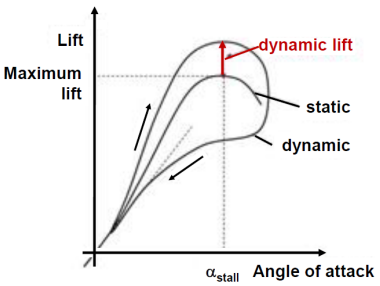

(a) Water tunnel visualization of vortex breakdown with illustration of out-of-phase spiral breakdown [14], (b) Static and dynamic normal force coefficient

Figure 8 – Vortex breakdown and maximum lift, static and dynamic

3.2.1 Static and dynamic lift: CL-α diagram

Figure 8b illustrates the phenomenon of "dynamic lift" for a pitching delta wing: in the upstroke motion, more lift is created than for the static wing at the same α because the breakdown location lags (i.e., is further downstream) that of the static position. This hysteretic lift behaviour creates a hysteretic loading of the wing with an overshoot of the static forces in the upstroke motion and an undershoot in the downstroke motion. The advantage of a rapid pitch-up maneuver for an aircraft is obvious with the additional normal force obtained compared to the static case, the so-called "dynamic lift" effect. This hysteresis effect is explored in section 5.2 and Figure 20.

4 F-16XL – a flying aerodynamics laboratory

Working in conjunction with NASA, General Dynamics aircraft designer, Harry Hillaker, (also responsible for the original F-16 design), devised the new hybrid cranked-arrow wing design for the F-16XL aircraft built for high-speed research as a stretch of the standard F16 (Figure 9). The wing modification aimed at improved supersonic and preserved transonic performance. NASA instrumented the F-16XL to provide a wealth of flight data, including pressure maps through the transonic speed range that provided a unique opportunity for CFD correlation and code validation with flight and wind tunnel data [15].

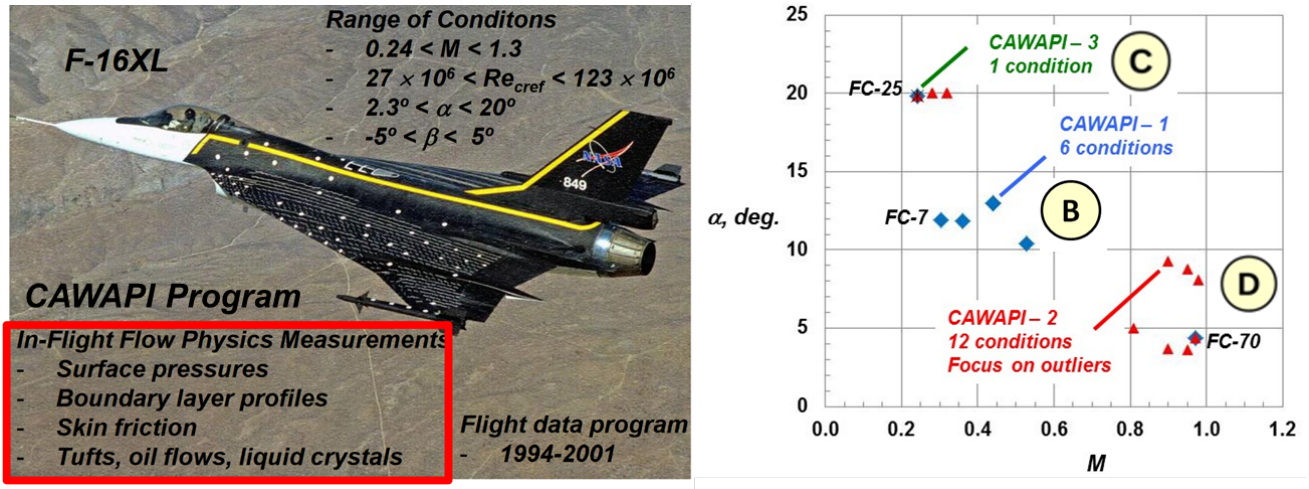

a) Flight data program b) flight test conditions M_∞ vs α

Figure 9 – F-16XL research aircraft – flying laboratory for CAWAPI Program [16]

The AVT-113 [16] Cranked Arrow Wing Aerodynamics Program, International (CAWAPI), focused on assessing CFD predictions of separated flows over the F-16XL aircraft (Figure 9a) against flight data that had previously been obtained by Lamar [15]. The flight conditions (Figure 9b) include:

(i) cruise condition B– suite of moderate angle of attack and moderate Mach number conditions
(ii) near-stall maneuver condition C– low-speed, high-angle-of-attack conditions
(iii) high-speed condition D– transonic, low-angle-of-attack.

The test-flight cases) are known to be challenging for CFD, and numerical (grid) effects were investigated to isolate the physical modeling effects. Several well-researched RANS turbulence models in common use were compared with unsteady hybrid RANS–LES modeling. Overall, the differences were not very significant in cases B, but become substantial in flight conditions C and D, known as *outlier* cases, reported here for flight conditions FC-70 and FC-25.

4.1 High-Speed condition D– Transonic, low α– FC70

The flight condition, FC-70, we consider is the high subsonic free stream Mach number $M_\infty = 0.97$ at the small angle of attack $\alpha = 4.3^\circ$ and $Re_{MAC} = 88.8M$. At this low angle of attack, the vortices do not dominate the flow field as they would at high α, but 3 shock waves are substantial in Figure 10(left). The iso-total pressure contours in Figure 10(right) show vortical layers over the wing, indicating that separation does

occur, but the lifted- off shear layer appears to remain close to the upper surface, just above the boundary layer [17].

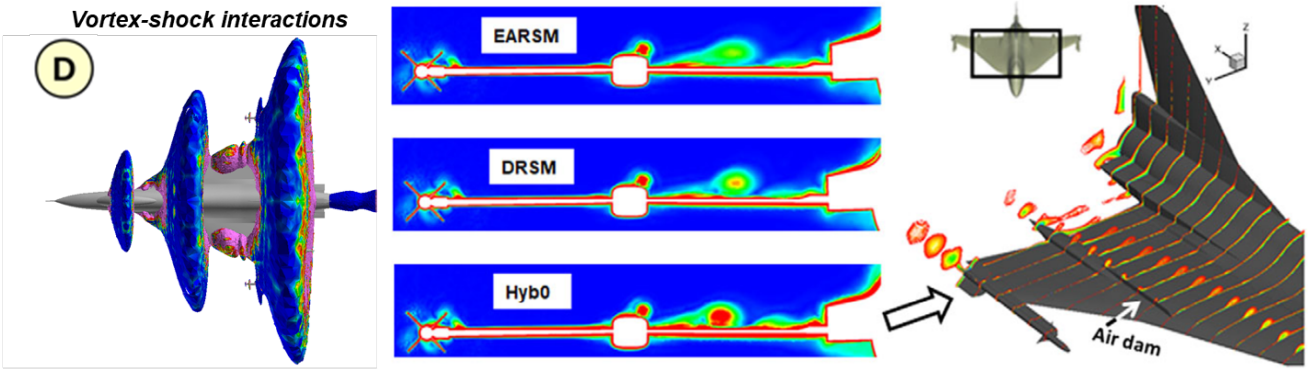

Figure 10 - Vortex-strength sensitivity to physical modeling, Edge code. CFD results for FC-70: M = 0.97, R_{cref}= 89 × 10^6, α = 4.4 deg (left). Vorticity magnitude in FS492 spanwise cut plane (center): EARSM + H. *k* – ω model (top); DRSM (center); Hyb0 (bottom). Iso-curves of total pressure in several body axis normal cuts (right), FS492 station indicated by large arrow.

Figure 10 (center) compares the vorticity magnitudes of the solutions from the EARSM, the k – ω DRSM, and the hybrid RANS–LES model Hyb0 physical modeling on the spanwise cut plane FS492 indicated by the arrow. Three vortices appear. The leading-edge vortex lifts off from the boundary layer between the fuselage and actuator pod on the inner wing panel, the actuator pod vortex is shed from the air dam, and the wing tip missile vortex is associated with the multiple lifting surfaces there. The models show little difference on missile and actuator pod vortices, but they do show difference on the inboard wing panel vortex. It separates from a smooth surface, so its "birth" is sensitive to turbulence modeling. The actuator pod vortex is created by the air dam, whose sharp edges define the separation. It is clear that the Hyb0 model preserves the vortex much further downstream compared to the other two models, giving a better preserved surface pressure footprint and a higher suction peak over the inner wing.

4.2 Near-stall maneuver condition C - low-speed, high α- FC25

4.2.1 Steady flow: secondary vortex separation- RANS simulation

The primary vortex in Figure 11 induces a low-pressure trough on the wing surface directly under it and the resulting pressure gradient causes the boundary layer to separate from the smooth surface into a *secondary vortex* that grows stronger with larger angles of attack. Elmiligui et al.[18] demonstrated improved secondary vortex predictions for flight condition FC-25 through a combination of grid resolution and turbulence model assessments that achieved the improved secondary vortex resolution with correspondingly improved correlations with the flight test data.

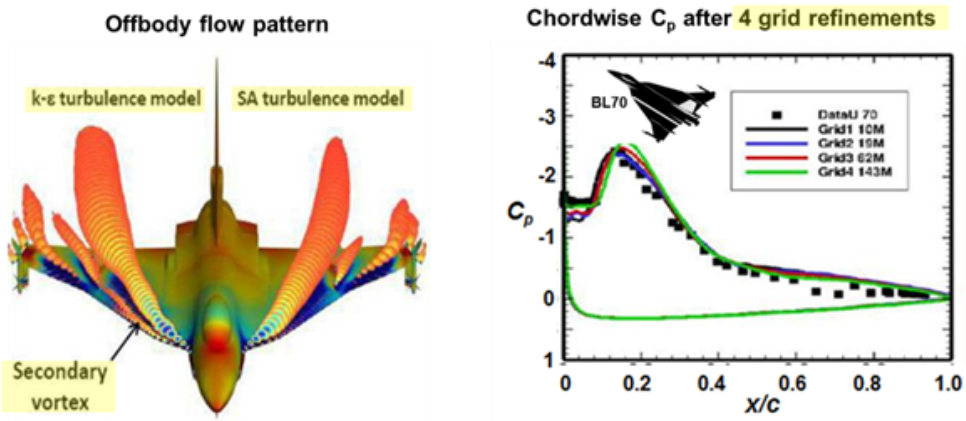

Figure 11 - Secondary vortex predictions, *FC-25: M* = 0.24, Re_{cref} = 32 x 10^6, α = 19.8°, [18]

In this case, the improved predictions came from the k-omega turbulence model, and it was not clear why this model produced the improved secondary vortex simulation while the Spalart-Allmaras (SA) model yields no secondary vortex even after substantial grid refinement. These findings demonstrated that difficulties remain in modelling sensitivities for resolving the separated vortex flows at differing scales with well-established turbulence models. The secondary vortex difficulties could relate to emergent shear-layer separation flow physics as we discuss with the diamond wing study below.

4.2.2 Unsteady flow: Vortex Breakdown – Hybrid RANS-LES simulation

One of the major findings of the CAWAPI-2 work, summarized by Rizzi and Luckring [19], is that unsteady flow, possibly with the vortex breaking down over the outer wing panel, occurred in the high-alpha case, *FC-25*. CAWAPI-3 studied this question further with Hybrid RANS/LES simulations, and results are summarized here.

Six independent assessments, using five hybrid RANS/LES methods showed detailed vortical content and substructure, including stronger secondary vortices than observed in steady RANS. For example using a standard *Q* criterion in Figure 12, Tomac et al [20] present an isometric view of vorticity colored by the pressure coefficient where the dark blue primary vortex from the inner, 70° swept wing is clearly evident. Slightly outboard of this vortex is a lighter blue-green secondary vortex structure. Further outboard, a tertiary vortex lies close to the leading edge. These secondary and tertiary vortices are small, and they are not commonly seen as distinctly as in these hybrid RANS/LES results

The primary vortex (dark blue) appears to burst over the trailing edge, and the secondary vortex seems to merge with the dark blue air dam vortex (both are counterrotating). On the outer, 50° swept-wing panel, a new leading-edge vortex (dark blue) is seen; and further outboard, this vortex merges with several smaller vortical structures from the tip missile, all of which breakdown over the trailing edge. The vortex breakdown phenomenon creates turbulent kinetic energy that must be modelled properly or be resolved. Many turbulence models create orders of magnitude too much turbulent eddy viscosity in the primary vortex core, which significantly alters the flowfield, and in some cases, eliminates breakdown observed experimentally at high Reynolds numbers.

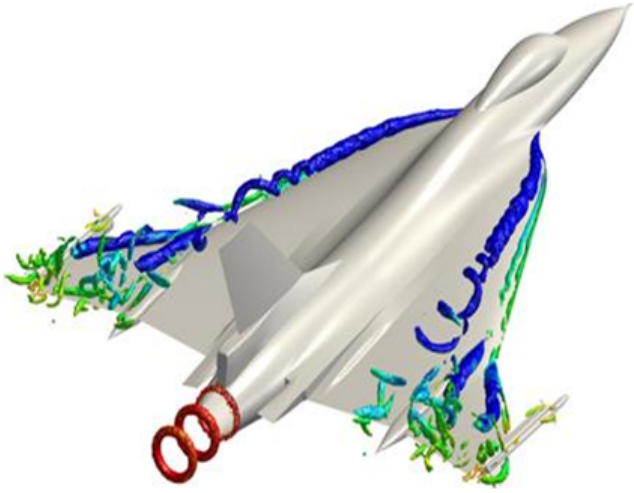

Figure 12 - Vortical flowfield over the F-16XL with vortex burst over the outer wing panel near the trailing edge [20]. Hybrid RANS/LES simulations, *FC-25*, $M = 0.242$, $Re_{cref} = 32.22 \times 10^6$, $\alpha = 19.84°$.

4.3 Incipient vortex separation from smooth edge

Let us study in more isolated detail, and in WT measurements, the weaknesses shown in the F-16XL simulations above, namely prediction of:

- Smooth-surface separation

– Vortex bursting, static and dynamic

The example comes from an STO collaboration identified as AVT-183 [21]. This work focused on a 53° swept diamond wing with a blunt leading edge. Figure 13(left) with fully turbulent computations from Frink et al. [22] shows the incipient separation region. The inner vortex was found to originate at the downstream limit of the insipient separation region, and Hitzel [23] first postulated its physics. The longitudinal location of incipient separation along the leading edge was found to be critical to good correlations between CFD and experiment. However, the progression of the separation with angle of attack was not consistently predicted among the CFD results from AVT-183, due to sensitivity in the turbulence model selected.

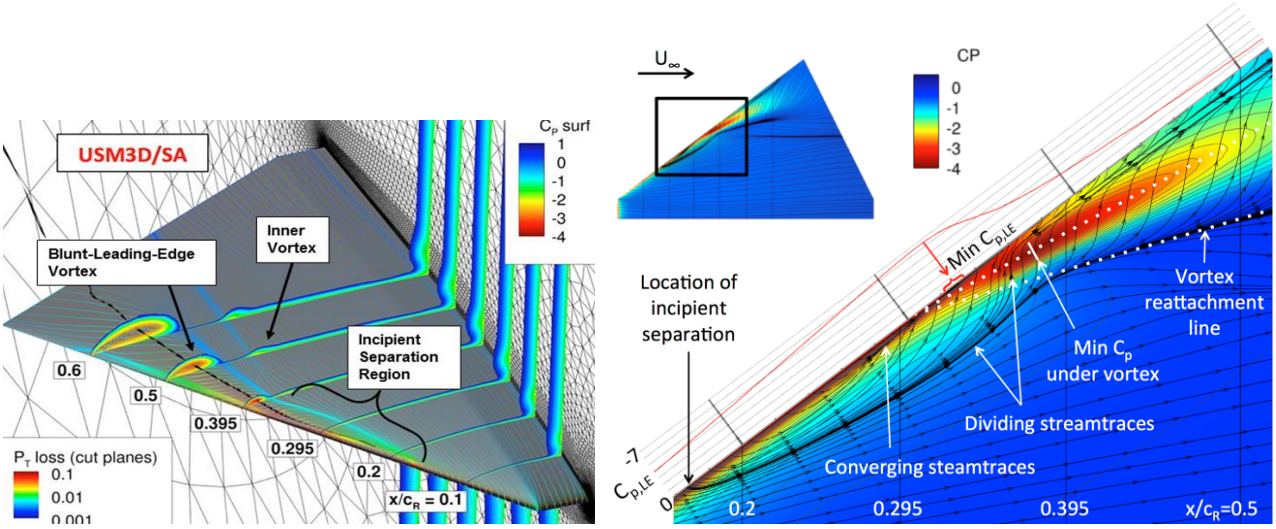

Figure 13 - Incipient separation, α = 12° Diamond wing, Λ_{le} = 53°, M = 0.15, Re_{mac} = 2.7 × 10^6. [22]

Frink et al. [22] observed a significant effect of the turbulence models where the location of the initial separation region (Figure 13 right) occurs progressively more inboard and forward along the leading edge for the KW-SST and EARSM turbulence models, relative to the SA result. With this strong sensitivity of turbulence models on the location of incipient separation, both here and in the other AVT-183 studies, no one model can be deemed better than another at this point in time, thus again the need for better physical modelling.

4.4 Vortex breakdown – static

In his PhD thesis, Görtz [24] computed full-span DES solutions for a 70° full-span delta wing, M = 0.2, Re_{cr} = 1.56 10^6, Λ = 27°, and extracted the vortex breakdown locations x_{vb} by determining the point along the vortex axis where the chordwise component of velocity equals zero.

Figure 14 left compares the breakdown locations computed at separation to experimentally measured values by Mitchell [25]. The circles in the plot are the mean measured breakdown locations, the dashed line is a quadratic curve fit to these, and the solid line with crosses gives the minimum and maximum break-down locations measured. The computed vortex breakdown locations range is 0.789 < x_{vb} /c_r < 0.813 for the port side and 0.769 < x_{vb}/c_r < 0.797 for the starboard side.

The simulations capture the mutual interaction between the port and starboard vortices, Figure 14 right. Spiral-type vortex breakdown predominates. Transformation from spiral- to bubble-type breakdown occurs and is associated with a significant upstream movement of the breakdown location, resulting in asymmetry between the port and starboard breakdown locations. The breakdown location fluctuates, and the asymmetry is responsible for low frequency oscillations in the aerodynamic coefficients, Figure 14 right. The sense of the spiral is opposite to the direction of rotation of the upstream vortex. The spiral

breakdown structure shows good qualitative agreement with the spiral-type breakdown over delta wings observed in experiments. Quantitative agreement, however, would require better physical modelling.

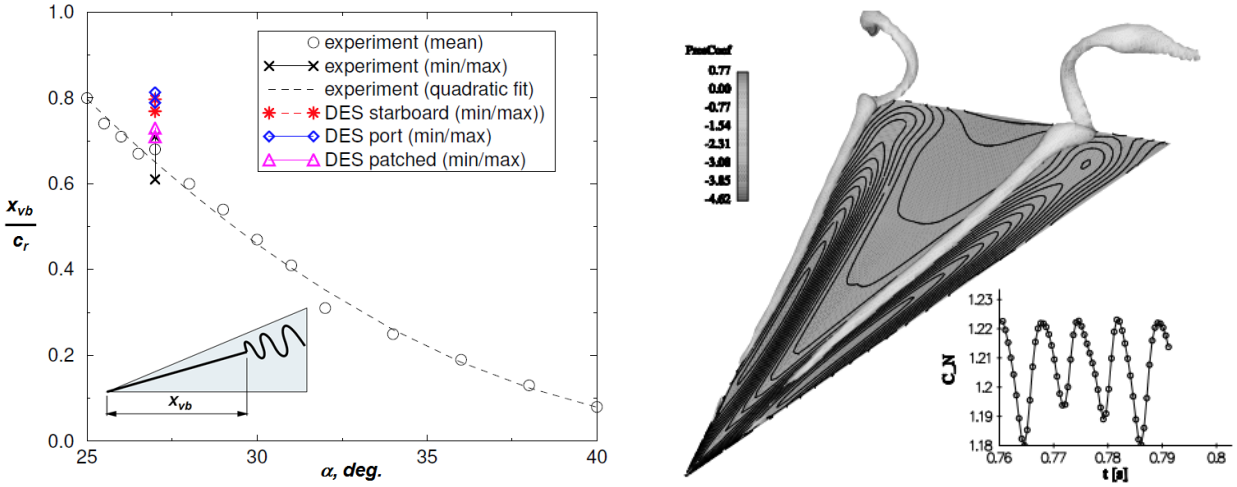

Figure 14 - Computed vortex breakdown locations [24] compared to Mitchell's experimental data [25], $\alpha = 27°$.

4.5 Vortex breakdown - dynamic

Lemoigne [26] has studied dynamic stall with vortex breakdown in his PhD thesis with computations of a forced-motion sharp-edge delta wing undergoing pitching dynamics consisting of sinusoidal oscillations defined by the angle-of-attack $\alpha(t) = 22° + 18° \sin(\omega t)$ with axis of rotation at $x/c = 0.4$. A static computation at the mean angle of attack is used as the starting point for the pitching computation. Figure 15a plots the computed RANS and Euler results for the normal force coefficient compared to experimental measurements by Brandon [27]. The maximal normal force is almost the same for turbulent and inviscid calculations and, in both cases, is higher than the experimental value, indicating that the prediction of dynamic vortex breakdown is difficult, even for a simple delta wing like this.

Figure 15b-c shows two views of the vortex above the wing at the same angle of attack, $\alpha = 22°$, but at different times in the oscillation cycle *n*. The wing is coloured by pressure and the zone of low pressure is visible below the vortex, an isosurface of total pressure. The figure qualitatively compares the shape of the vortex and the position of the breakdown on the upstroke (Figure 15b) with that of the downstroke (Figure 15c) at 22° angle of attack. The sudden bulging out of the isosurface marks the instantaneous location of where the vortex breaks down, and its motion varies greatly over the oscillation in pitch.

On the upstroke, Figure 15b, the breakdown location moves upstream but clearly lags behind the static position (i.e. trailing edge). On the downstroke, Figure 15c, the breakdown location is near the quarter root-chord location over the wing, moving downstream, leading its static position. These dynamic results are in sharp contrast to the static case where breakdown at the trailing edge occurs at $\alpha = 22°$. They show the distinct lag in the breakdown position during both the upstroke and the downstroke of the delta wing. The same type of hysteresis effects are seen in the pitching wing simulation results presented in section 5.2

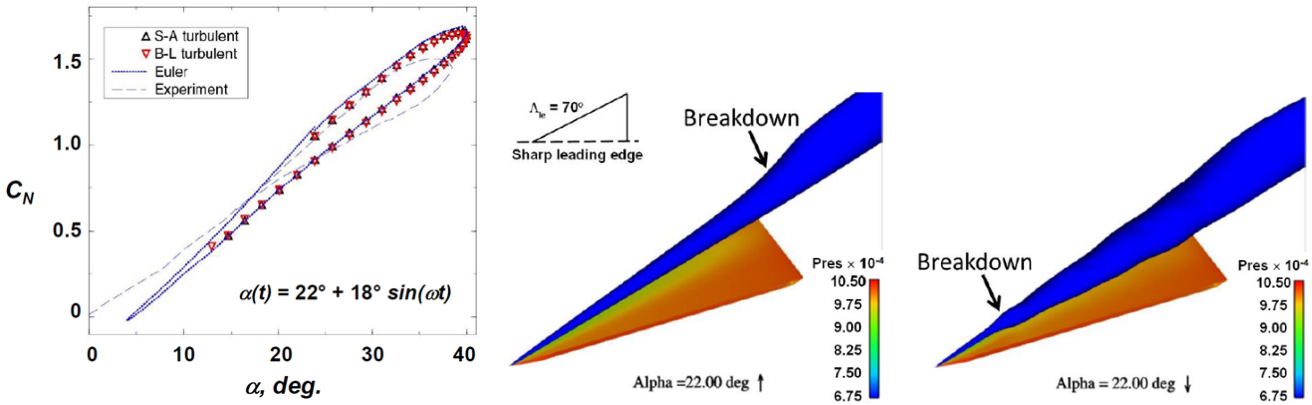

(a) Normal force coefficient C_N versus angle of attack $\alpha\ (t)$

b) $\alpha\ (t) = 22^o$ during upstroke at $\omega t = 2n\pi$

(c) $\alpha\ (t) = 22^o$ during downstroke at $\omega t = (2n+1)\ \pi$

Figure 15 - Hysteresis effect on vortex breakdown for an oscillating delta wing. URANS/SA, $M = 0.2$, $Re_{cr} = 3.16 \times 10^6$, $\alpha_0 = 22°$, $\Delta\alpha = \pm 18°$ at $\omega = 5.12$ rad/sec.

5 Turbulence-resolving methods: Direct numerical simulations and the virtual wind tunnel

Just as applied CFD has evolved greatly over the last decades, so has also the direct numerical simulations. At this point there is a possibility to perform turbulence resolved detailed simulations of aeronautically relevant flows. When Landahl in 1990 showed DNS of low Reynolds number turbulent channel flows, now we can perform simulations of flows similar to those studied in university wind tunnels. We call these simulation capabilities the virtual wind tunnel. In the same manner, Landahl showed simple stability calculations of channel flows, where we below show stability of realistic leading edge separation bubbles. These studies can reveal some of the fundamental physics involved with leading-edge vortex separation as envisioned in the sketches in Figs 7 and 8 in Section 3.1.1 above.

Here we discuss some recent examples of direct numerical simulations of separated flows of aeronautical interest. We cannot choose the full aircraft configuration for such simulations, but we have been able to move towards unsteady airfoils and wings and simulate flows where traditional CFD methods have largely failed. First, we show pitching wings, both with and without leading edge separation and then as an outlook we briefly consider dynamic stall and turbulent wingtip vortices from finite wings.

5.1 Pitching wing with leading edge separation at a low Reynolds number

Figure 16 (left) shows the iso-contours of instantaneous vortical structures at four different time instants during the pitch-up cycle when the transition is moving upstream and on the right from top to bottom shows the part of the oscillation cycle when transition is moving downstream. During the upstream phase a leading-edge laminar separation bubble (LSB) appears and grows in size and suddenly causes transition to move all the way up to the end of bubble. During the downstream phase the flow is mostly laminar across the airfoil with no structures observed prior to flow transition (close to trailing edge) and there is no leading-edge LSB. The high adverse pressure gradient near the trailing edge causes the laminar flow to easily separate, forming a separation and the flow transitions over this separated shear layer.

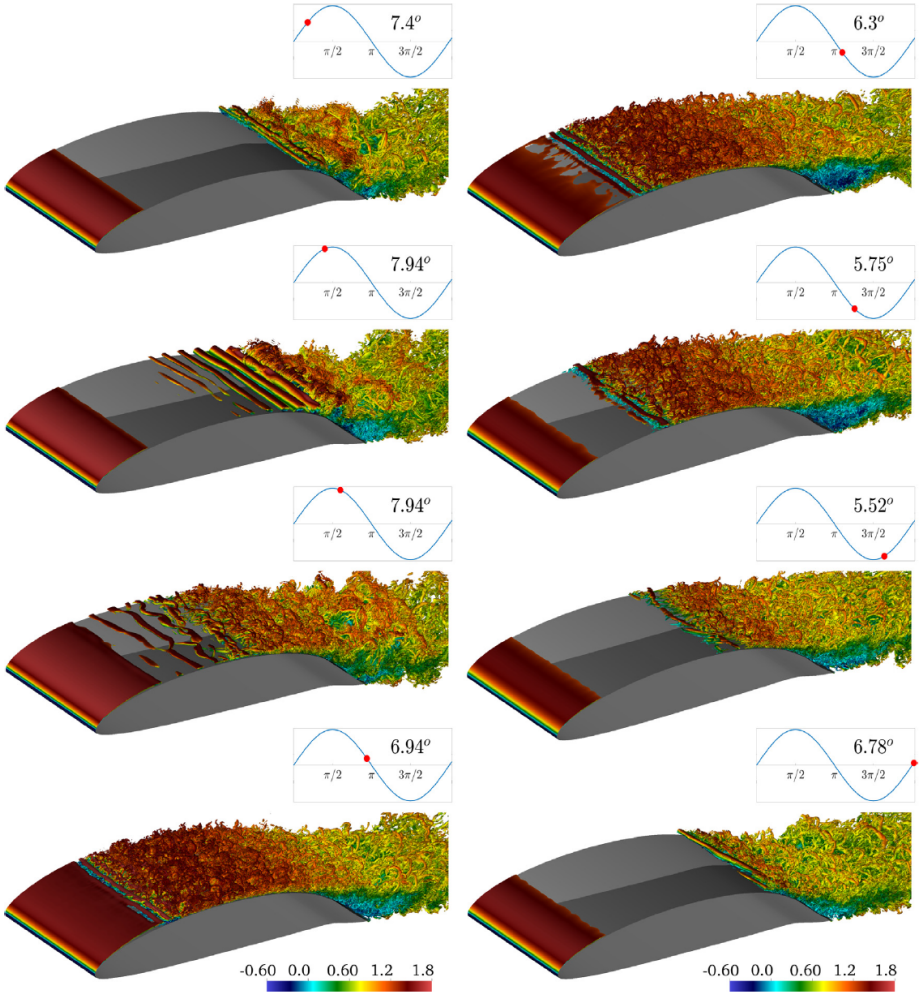

Figure 16 – Pitching wing cord Re=100.000, note that there is a hysteresis so that the maximum and minimum laminar flow occur at about the average angle of attack instead of at the maximum or minimum. Negi et al. [28].

The spatio-temporal variation of the boundary layer can be analyzed via the instantaneous wall shear stress. Figure 17 (left) shows the space-time variation of the instantaneous, spanwise averaged wall shear stress on the suction side of the airfoil surface. There is a marked asymmetry between the upstream and downstream movement of the transition point. An approximate velocity for both the upstream and downstream motion of the transition point can be estimated from the slopes of the transition lines in figure 17 (right). The velocity of upstream transition movement is about Vtr = –0.60, while the velocity of the downstream motion of transition is about Vtr = 0.17. Thus, the upstream spread of turbulent regions is much faster than flow re-laminarization.

We identify some of the key boundary-layer characteristics and find an over-all picture of the dynamics in Figure 17. A persistent trailing-edge separation can be identified in the left figure beyond $x/c > 0.8$. The trailing-edge separation does not exhibit reverse flow during all times, as can be seen from the white patches dispersed between largely black colored regions. An isolated separated region (distinct from the trailing edge separation) is observed at $x/c \approx 0.6$ at times $t/Tosc \approx 3$ and $t/Tosc \approx 4$. This is identified as a trailing-edge laminar separation bubble (LSB). This LSB is short-lived in time, existing for slightly less than a quarter of the pitch-cycle. A large separated region near the leading edge is a leading-edge LSB, which persists much longer in time, spanning nearly half a pitch cycle.

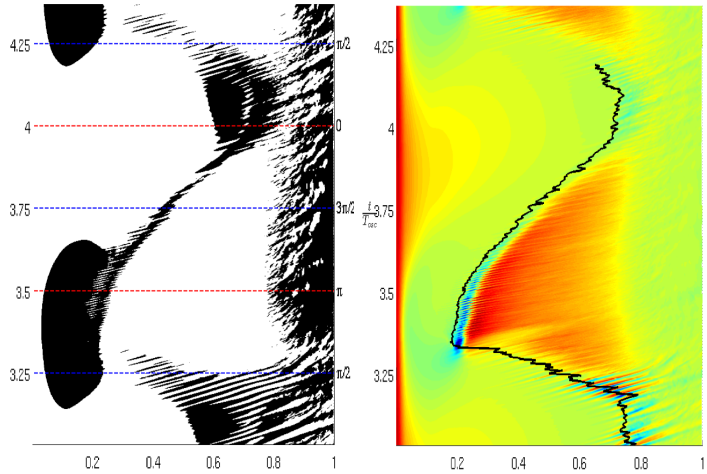

Figure 17 – Separated regions and wall shear stress as a function of time. Left figure shows areas of separated flow and right figure shows transition location and regions of high (red) and low (green) shear. Negi et al. (2018) [28].

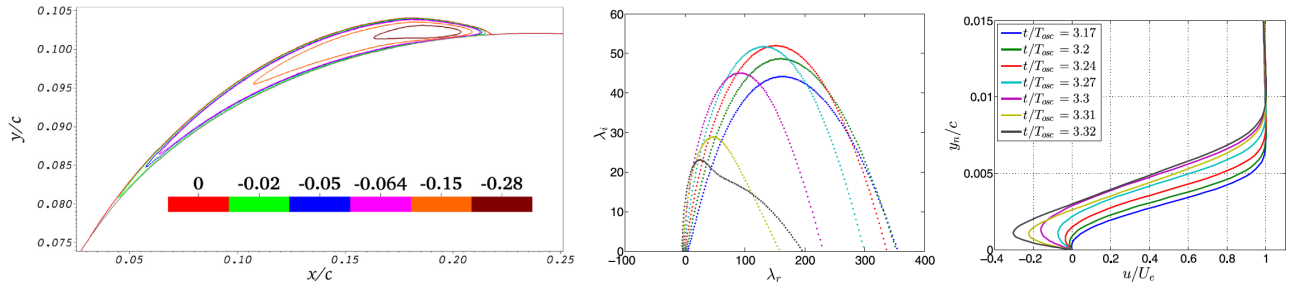

Figure 18 – Left: negative velocity contours of the leading-edge separation bubble at t/T_{osc}=3.33. Middle: instability growth rates (ω_i) as a function of angular frequency of perturbations (λ_r). Right: mean profiles in the bubble for indicated times. From Negi et al. [28].

The leading-edge separation bubble is investigated during its maximum extent where its instability is analysed. Figure 18 shows the unstable complex frequencies obtained from the temporal stability analysis (with varying streamwise wavenumber kx) for instantaneous profiles at several different time instants in the fourth pitch cycle. The reverse-flow intensity continues to increase with time until flow transition occurs at the LSB. The flow is unstable for all the analyzed velocity profiles as shown by the existence of complex frequencies with a positive imaginary part. However, the highest amplification rate (frequency with maximum imaginary part) does not monotonically increase with reverse-flow intensity. At first the maximum amplification rate increases in time, but later it is seen to decrease. These changing characteristics can be associated with structural changes in the LSB, where at first the region of maximum reverse-flow is found near the center of the LSB, but as the LSB grows, this region of strong reverse flow moves closer to the downstream end of the LSB. Such qualitative changes in the shape of the LSB can be observed in figure 18.

Further analysis in Negi et al. [28] shows that the drastic change in transition location on the airfoil is associated with a so-called absolute instability, where the group velocity of the instability waves approach zero and there is an explosive growth at the location of the origin of the instability. Such a detailed analysis was possible due to the well resolved DNS solution so that sharp shear layers inside the bubble, which determines the stability characteristics, could be determined with high accuracy. This shows the potential of large scale accurate direct numerical simulations to elucidate complex flow physics in aeronautically relevant flows.

5.2 Pitching wing at a larger Reynolds number

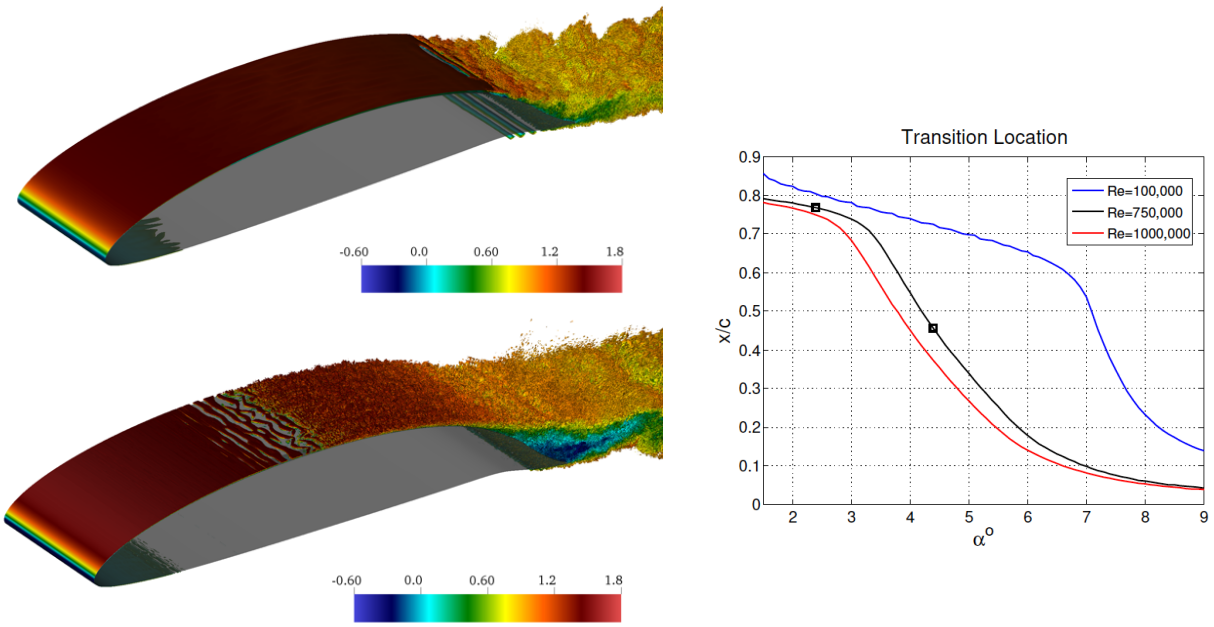

Figure 19 – Solution at constant values of the angle of attach for the lowest and highest values in the pitching motion, Re=750.000. Right figure: variation of the transition location with the angle of attack. The two squares indicate the transition location for the two simulations on the left. From Negi et al. [29]. The red line shows experimental results from Lokatt [30].

The results shown in figure 19 is from a collaboration between SAAB and aeronautics and mechanics researchers at the Engineering Mechanics Department at KTH and was performed within the national aeronautics program funded by Vinnova. The motivation was to understand the large movement of the transition location for some long endurance aircraft of interest to SAAB. The movement of the transition location influenced the aerodynamic forces and could potentially affect the control of the aircraft.

These studies were made at higher Reynolds numbers. In the simulations we considered a Reynolds number of Re=750.000, where the leading-edge separation bubble disappears compared to the lower Re described earlier, but the sensitive motion of the laminar-turbulent transition remains, see Figure 19. A separation at the trailing edge also remains as can be seen from the shear stress evolution. Figure 19 from Negi et al. [29] shows the instantaneous vortical structures for two angles of attack of 2.4 and 4.4 degrees. The pitching motion will occur in between these values. Turbulent regions can be identified by the presence of small-scale structures. It is clear that the transition occurs at widely different chordwise locations for the two angles of attack.

The spatiotemporal variation of the boundary layer can be analysed via the instantaneous wall shear stress. Figure 20 (left) shows the space-time variation of the instantaneous, spanwise averaged wall shear stress on the suction side of the airfoil surface. Areas which are strongly red in colour are high shear stress regions and thus signify turbulent flow (except the region very close to the leading edge, which has a very thin boundary layer). The yellow to green regions indicate very low or negative shear stress regions and the magenta line represents the transition location. The turbulent regions show periodic bumps in the space-time plot which are indicative of the movement of transition throughout the oscillation phases. Changes in trailing-edge separation accompany the variation in laminar-to-turbulent transition point. Trailing-edge separation is absent when the transition is at its most downstream location, while a large separated region develops when the transition is at its most upstream location.

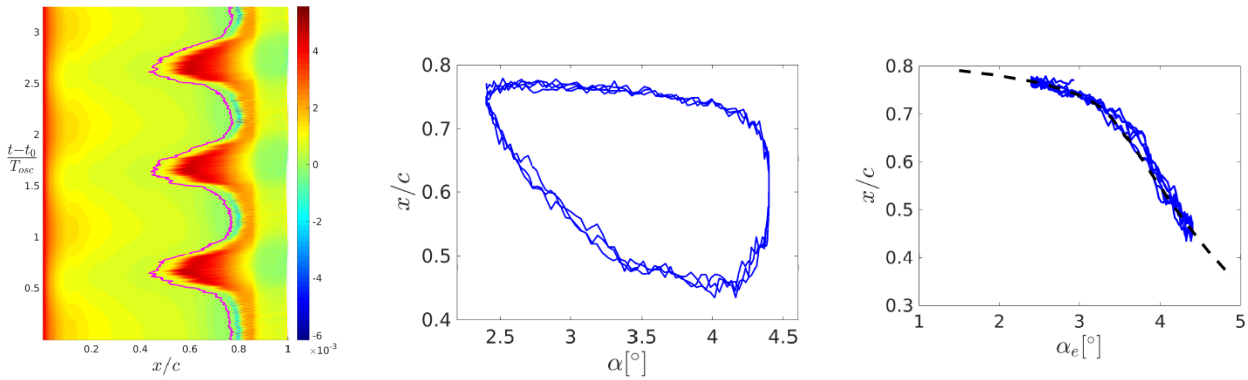

Figure 20 – Overall shear stress evolution as a function of time and changes in transition location as a function of the angle of attack (without and with phase lag). Note that with a phase lag the hysteresis in the transition location is removed. From Negi et al. [29].

The variation of transition location with the instantaneous angle of attack is also shown in Fig. 20 (right figures). The plot clearly shows the asymmetric flow states between the pitch-up (upper branch) and the pitch-down (lower branch) phases of the oscillation. During the pitch-up phase, the transition point is near the trailing edge and has a very slow upstream movement for most part of pitch-up cycle and later moves upstream sharply at the end of the pitch-up phase. During the pitch-down phase of the oscillation, the transition location is constantly moving downstream with the motion appearing much more gradual in phase space.

This plot can be transformed to give a more insightful picture of the ongoing dynamics by using a phase-lag concept. In this transformation, we consider the evolution of the boundary layer with respect to an effective angle of attack, which differs from the instantaneous angle of attack by a phase lag. The physical interpretation of the phase lag is a simple one, i.e. the boundary layer adjusts to the changing flow-field in a quasi-steady manner however, there is a lag between the airfoil motion and the boundary-layer adjustment, and the effective angle of attack that the boundary layer perceives is different from the instantaneous angle of attack. The observed hysteresis type behaviour with respect to the angle of attack can almost entirely be explained by the phase-lag concept, see left figure in Figure 20.

A model has been devised based on this phase-lag concept and applied to the experiments of Lokatt [30]. The model was able to predict the non-linear response of the lift coefficient seen in her KTH experiments. This is another example where the detailed DNS could help elucidate complex flow physics in aeronautically relevant flows.

5.3 Outlook: toward more complex separated flows

As an outlook to what type of direct numerical simulation that is now becoming feasible, we present DNS simulations from the KTH group of dynamic stall and a turbulent wing tip vortex, both being simulated with the Nek500 software.

5.3.1 Dynamic stall

In Figure 21 snapshots in time of an NACA0009 airfoil that is pitching up from 8 degrees to 24 degrees are shown. This is a flow case is similar to one that has been simulated with somewhat coarser LES methods earlier (Visbal and Garmann 2018) [31], while here it is for the first time computed with DNS in order for all of the detailed flow physics to be captured. The overall development of the flow can be seen in the space-time diagram of the wall shear-stress on the suction side of the airfoil, shown in the left part of the Figure 21.

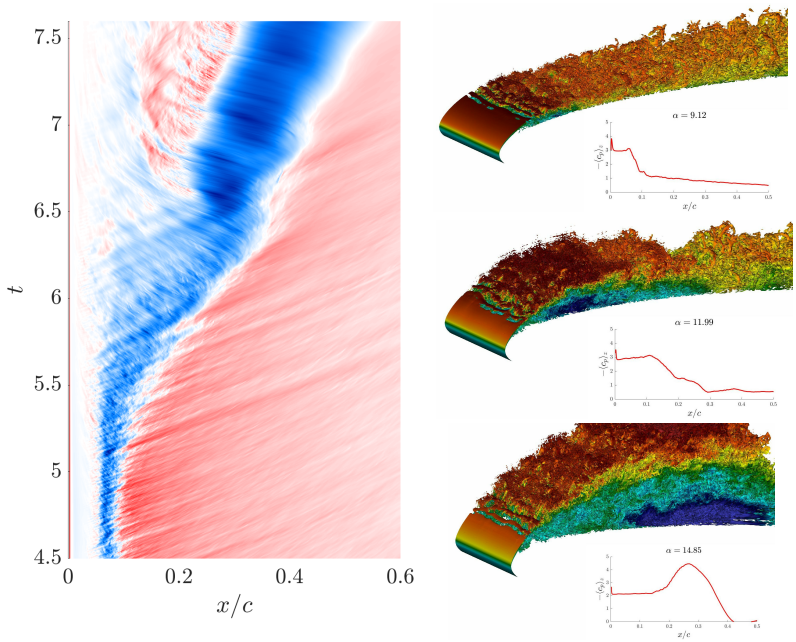

Figure 21 – Dynamic stall simulation at Re=200.000. Left: shear stress as a function of time, blue negative and red positive. Right: Snapshots of the turbulent flow field (lambda_2 iso-surfaces coloured by streamwise velocity) at angles of attack 9.12, 11.99 and 14.85 degrees, showing the development of the large separated region and the downstream motion of the dynamic stall vortex. From Kern et al. [32]

The large blue negative shear stress area bending to the right represents the laminar separation bubble at the leading edge that rolls up into the stall vortex and moves over the wing. Note the backward moving disturbances under the vortex on the wing surface. To the right in Figure 21 we see three snapshots of the flow, from the largely attached flow (top) to an enlarged leading-edge bubble and subsequently to the large stall vortex (bottom). The inset shows the instantaneous spanwise-averaged pressure coefficient at the leading edge. Note the large extension of the turbulent flow above the wing during the late part of this process. The aim of this project is to find details of the flow physics responsible for the bursting of the separation bubble and the subsequent formation of the dynamic stall vortex, providing the resolved physics of the flow sketched in Figure 6.

5.3.2 Finite wing with wingtip vortex

Next, we turn to a recent simulation showing important new capabilities for DNS of aeronautical flows. We consider finite wings where we need to resolve the complex flow physics of the turbulence on the wing with the generation and evolution of the wing-tip vortex, see Figure 22.

In Figure 22 we see a turbulent wing, modeled as a NACA0012 profile with a rounded wing tip, at an angle of attack of 5 degrees (case denoted by RWT5). The figure shows the emergence of the wing-tip vortex, as well as the computational mesh at various downstream positions. In order to minimize the computer time needed while keeping the accuracy of the simulation, an adaptive-mesh-refinement (AMR) procedure has been implemented into the Nek5000 simulation software. Thus, the grid has been refined close to the surface of the wing in the area of the turbulent flow, but also in the freestream behind the wing tip around the strong wing-tip vortex. The final grid is generated by iterative refinement of the initial grid, where the elements with the highest contribution to the error at each iteration are refined. In this manner, a highly complicated flow over a complex geometry can be simulated using direct numerical simulations.

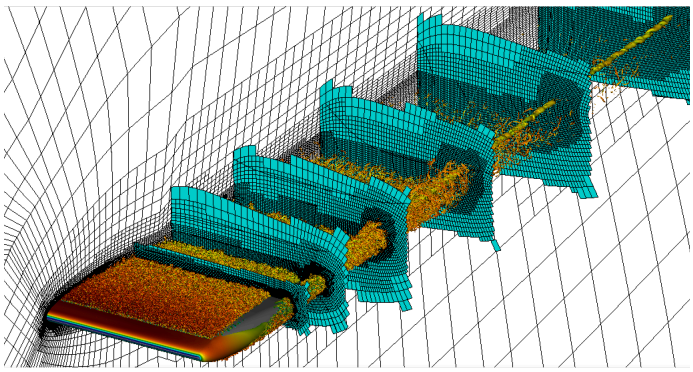

Figure 22 Spectral-element grid for case RWT5 with 3.1million spectral elements. The grid is generated using the h-adaptation capabilities of the AMR (adaptive mesh refinement) version of Nek5000. We show instantaneous vortical structures represented by λ2 isosurfaces colored by streamwise velocity ranging from (blue) low to (red) high. From Toosi et al. [33]

These new capabilities in generating and optimizing grids will be of paramount importance in future studies of flows around more complex geometries and involving complex flow physics needing high resolution computations. In addition, the details of the tip vortices will be explored further in coming publications and at this stage represent work in progress.

6 Path Forward to Better Physical Models and Conclusions

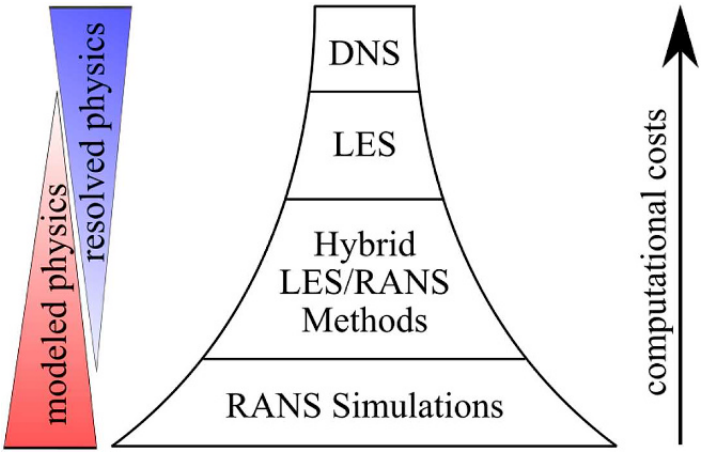

Figure 23 - The hierarchy of turbulence modeling approaches. Figure inspired by Sagaut et al. [34]. Abbreviations: DNS, direct numerical simulations; LES, large eddy simulations; RANS, Reynolds-averaged Navier–Stokes.

We end the paper with an example of how DNS studies could help the deficiencies identified in the first part of the paper. Figure 23 shows a hierarchy of turbulence formulations and illustrates the two parts of this paper where Part 1 we discussed RANS and hybrid RANS-LES methods and Part 2 where we discussed turbulence-resolved DNS/LES methods.

6.2 The HiFi-Turb EU Project

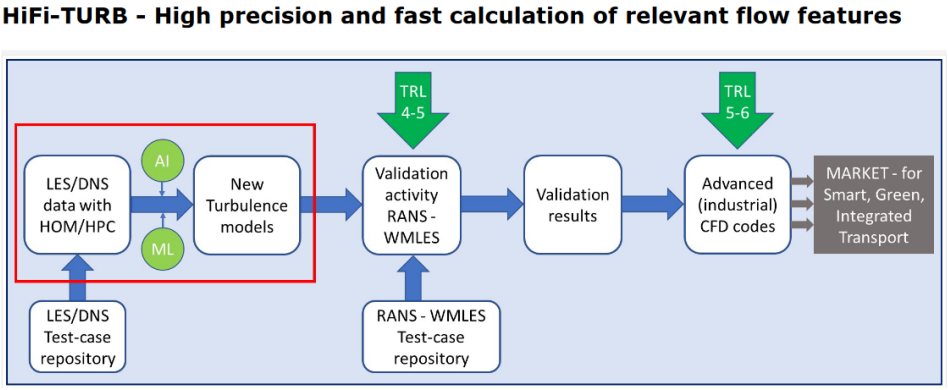

Figure 24 – Workflow in EU HiFi-turb project

Within the EU program Horizon 2020 the German Aerospace Center (DLR) and the partners evolve in the project HiFi-TURB (High-Fidelity DNS/LES for Innovative Turbulence Models) a new generation of reliable anisotropy-resolving turbulence models, able to predict accurately separated and vortical flows for the European aeronautics industry to be used in RANS and Hybrid RANS-LES methods – forming the CFD backbone in industry. With the innovative and ambitious objectives and goals of the HiFi-TURB project, using for the first time large and highly-refined LES/DNS data bases in a systematic manner, including the innovative use of AI and big-data technologies for feature detections towards new/improved turbulence models, the present gaps of capabilities in modelling challenging conditions within the flight envelop will be largely removed. According to the latter and driven by the work program and the technical objectives described above, industry will be supported and – to a certain extent – educated on how to run their simulations more 'automatically' with a minimum of user interventions – related to modelling aspects. Based on the present and even more future situation concerning HPC networks, it is the ambition of the HiFi-TURB project to forming the backbone in reaching the goals of resolving all relevant flow features in short times. The DLR-Institute of Aerodynamics and Flow Technology leads a Work Package in HiFi-TURB and is mainly engaged in deriving and investigating new turbulence model terms based on its expertise in turbulence. This is an important example of how detailed DNS simulations are used to devise better models for separated and vortical flows.

An example applying statistical inference and ML (Machine Learning) to turbulent flows over airfoils is shown below, Fig. 25. It shows streamlines and x-velocity contours for S809 airfoil at Re = 2 10^6 and alpha =14 deg using the Spalart-Allmaras (SA) turbulence model and its adaption by tuning with ML. Duraisamy et al. [35.]

6.2 Conclusions

Part 1 of the paper has described the progress and challenges in using available CFD tools, as seen from the industrial aero-space design point of view, and, as seen from the research front on high-performance computing requiring resolution of all scales, Part 2. In the foreseeable future, full-scale Re configurations are out of reach for DNS and improved design tools will rely on progress in physical modelling.

But the two communities implied by the two-part presentation are not on either side of some great divide. Instead, the DNS tools offer unprecedented quality and volume of data to help the modelers, as the understanding of flow mechanisms simultaneously expands. We see the engineering and academic communities rapidly joining forces in the quest for better theory, models, software and finally aerodynamics.

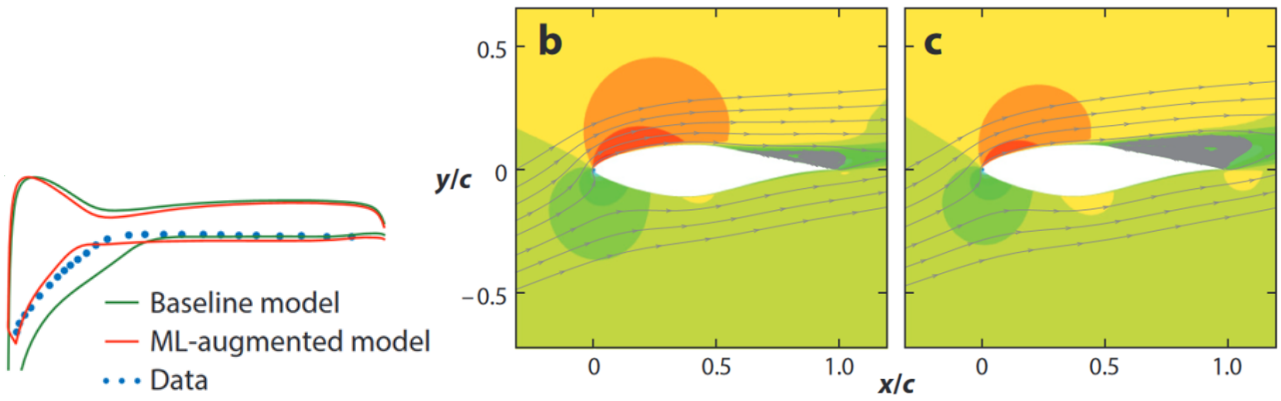

Figure 25 – Left: Pressure over an airfoil surface. Right: (b) Baseline SA flow and (c) Flow with data-driven SA model. Figure adapted with permission from Singh et al. [36]

Acknowledgements

We would like to thank our collaborators, Jesper Oppelstrup, James Luckring, Prabal Negi, Armin Hosseini, Simon Kern, Ricardo Vinuesa, Ardeshir Hanifi and Philipp Schlatter.

Copyright Statement

References

[1] Landahl, M.T. CFD and Turbulence, *Guggenheim Lecture, 17th ICAS Congress*, Stockholm, ICAS-Paper-90-0.1, 1990.

[2] Rizzi, A. and Luckring, J. Historical development and use of CFD for separated flow simulations relevant to military aircraft. *Aerospace Science and Technology*, Vol. 117, pp. 1-42, 2021.

[3] Spalart, P. R, and Venkatakrishnan, V., "On the Role and Challenges of CFD in the Aerospace Industry," *The Aeronautical Journal*, Vol. 120, No. 1223, 2016, pp. 209-232.

[4] Vos, J., B., Rizzi, A., Darracq, D., and Hirschel, E. H., "Navier–Stokes solvers in European aircraft design," *Progress in Aerospace Sciences*, Vol 38, No. 8, 2002, pp. 601-697.

[5] Hirschel, E. H., Rizzi, A., Breitsamter, C., and Staudacher, W. *Separated and Vortical Flow in Aircraft Wing Aerodynamics*, Springer Nature, Berlin, 2021.

[6] Spalart, P. R., Jou, W-H., Strelets, M., and Allmaras, S. R., "Comments on the Feasibility of LES for Wings, and on a Hybrid RANS/LES Approach," *Advances in DNS/LES, 1st AFOSR Int. Conf. on DNS/LES,* Aug 1997, Grey den Press, Columbus OH.

[7] Levy, D. W. and DPW Organizing Committee, *The CFD Drag Prediction Workshop Series: Summary and Retrospective*, https://cfd.ku.edu/JRV/Levy.pdf

[8] Luckring, J.M. and Boelens, O.J. A reduced-complexity investigation of blunt leading-edge separation motivated by UCAV aerodynamics, in: AIAA Science and Technology Forum and Exposition (SciTech 2015), AIAA Paper 2015-0061, January 2015.

[9] Hummel, D. The International Vortex Flow Experiment 2 (VFE-2): Background, objectives and organization, Aerospace Science and Technology 24, 2013, pp1–9

[10] Boelens, O.J. and Luckring, J.M. Numerical and theoretical considerations for the design of

the AVT-183 diamond-wing experimental investigations, in: AIAA Science and Technology Forum and Exposition (SciTech 2015), AIAA Paper 2015-0062, January 2015.

[11] Polhamus, E. C., "A Survey of Reynolds Number and Wing Geometry Effects on Lift Characteristics in the Low Speed Stall Region," NASA CR-4745, 1996.

[12] Küchemann, D., "Types of Flow on Swept Wings," *J. Royal Aero Soc.*, Vol. 57(515), 1953, pp 683-699.

[13] Rizzi, A., Oppelstrup, J.: *Aircraft Aerodynamic Design with Computational Software*. Cambridge University Press, Cambridge (2021)

[14]Lambourne, N.C. and Bryer, D.W. The bursting of leading edge vortices — some observation and discussion of the phenomenon, Aeronautical Research Council, R & M 3282, 1962.

[15]Lamar, J. E., Obara, C. J., Fisher, B. D., and Fisher, D. F., "Flight, Wind-Tunnel, and Computational Fluid Dynamics Comparison for Cranked Arrow Wing (F-16XL-1) at Subsonic and Transonic Speeds," NASA TP 2001-210629, Feb 2001.

[16] Lamar, J.E. Prediction of F-16XL Flight-Flow Physics, J Aircraft Vol. 46, No. 2, March–April 2009, p354

[17] Tomac, M. and Rizzi, A. Computational Fluid Dynamics Predictions of Control-Surface Effects for F-16XL Aircraft *J Aircraft* Vol. 54, No. 2, March–April 2017, pp395-408

[18] Elmiligui, A., Abdol-Hamid, K., Cavallo, P. A., and Parlette, E. B., "USM3D Simulations for the F-16XL Aircraft Configuration," *J Aircraft*, Vol. 54, No. 2, pp. 417-427, 2017.

[19] Rizzi, A. and Luckring, J.M.: What was Learned in Predicting Slender Airframe Aerodynamics with the F-16XL Aircraft, *AIAA Journal of Aircraft,* Vol 54, No. 2, pp. 444-455, 2017.

[20] Tomac, M. Jirasek, A. and Rizzi, A. Hybrid Reynolds-Averaged Navier–Stokes/Large-Eddy Simulations of F-16XL in Low-Speed High-Alpha Flight, *J Aircraft* Vol. 54, No. 6, November–December 2017, pp2070-2076.

[21] Luckring, J.M and Boelens, O.J. A Unit-Problem Investigation of Blunt Leading-Edge Separation Motivated by AVT-161 SACCON Research NATO RTO Specialists Meeting AVT-189, Rep. NF1676L-12101, 2011

[22] Frink, N. T., Tomac, M., and Rizzi, A., "Collaborative study of incipient separation on 53º-swept diamond wing," *Aerospace Science and Technology*, Vol. 57, 2016, pp76-89.

[23] Hitzel, S. M., Boelens, O. J., Rooij, M., and Hövelmann, A., "Vortex development on the AVT-183 diamond wing configuration – numerical and experimental findings," *Aerospace Science and Technology*, Vol. 57, 2016.

[24] Görtz, S., "Realistic simulations of delta wing aerodynamics using novel CFD methods," KTH PhD Dissertation, Rep Trita-AVE 2005:01, Stockholm, 2005.

[25] Mitchell, A. M., "Caractérisation et contrôle de l'éclatement tourbillonnaire sur une aile delta aux hautes incidences," Ph.D. thesis, Université Paris VI, Paris, France, 2000.

[26] LeMoigne, Y., "Adaptive Mesh Refinement and Simulations of Unsteady Delta-Wing Aerodynamics," KTH PhD Dissertation, Rep Trita-AVE 2004:17, Stockholm, 2004.

[27] Brandon, J. M. 1991, "Dynamic Stall Effects and Applications to High Performance Aircraft," AGARD-R-776 pp 2-1 2-15, 1991.

[28] Negi PS, Vinuesa R, Hanifi A, Schlatter P, and Henningson DS Unsteady aerodynamic effects in small-amplitude pitch oscillations of an airfoil. IJHFF 71, 2018.

[29]Negi, PS, Hanifi A and Henningson DS Unsteady Response of Natural Laminar Flow Airfoil Undergoing Small-Amplitude Pitch Oscillations. AIAA J 59, 2021.

[30] Lokatt, M., "On Aerodynamic and Aeroelastic Modeling for Aircraft Design," Doctoral Thesis, KTH Royal Inst. of Technology, Stockholm, 2017.

[31] Visbal, M.R. and Garmann, D.J. Analysis of Dynamic Stall on Pitching Airfoil Using High-Fidelity Large-Eddy Simulations. AIAA Journal, 56, 46-63, 2018.

[32] Kern S, Hanifi A and Henningson DS Direct numerical simulation of dynamic stall. Private communication, 2022.

[33] S. Toosi S, Peplinski A, Schlatter P and Vinuesa R THE EFFECT OF WING-TIP VORTICES ON THE FLOW AROUND A NACA0012 WING, DLES Workshop Udine, 2021.

[34] Sagaut, P., Deck, S. and Terracol, M.: Multiscale and Multiresolution Approaches in Turbulence, second ed., Imperial College Press, 2013.

[35] Duraisamy, K, Iaccarino, G, and Xiao, H.: Turbulence Modeling in the Age of Data, Ann. Rev. Fluid Mech. 51:357-377, 2019..

[36] Singh AP, Medida S, Duraisamy K.: Machine-learning-augmented predictive modeling of turbulent separated flows over airfoils. AIAA J. Vol 55, pp2215–27, 2017.